Entanglement distribution over a 96-km-long submarine optical fiber

Sören Wengerowsky[a,b,1], Siddarth Koduru Joshi[a,b,c,d], Fabian Steinlechner[a,b,e,f], Julien R. Zichi[g,h], Sergiy M. Dobrovolskiy[h], René van der Molen[h], Johannes W. N. Los[h], Val Zwiller[g,h], Marijn A. M. Versteegh[g], Alberto Mura[i], Davide Calonico[i], Massimo Inguscio[j,k,l], Hannes Hübel[m], Liu Bo[a,b,n], Thomas Scheidl[a,o], Anton Zeilinger[a,o,1], André Xuereb[p], and Rupert Ursin[a,b,1]

[a]Institute for Quantum Optics and Quantum Information–Vienna, Austrian Academy of Sciences, 1090 Vienna, Austria; [b]Vienna Center for Quantum Science and Technology, 1090 Vienna, Austria; [c]Quantum Engineering Technology Labs, H. H. Wills Physics Laboratory, Bristol BS8 1FD, United Kingdom; [d]Department of Electrical and Electronic Engineering, University of Bristol, Bristol BS8 1UB, United Kingdom; [e]Fraunhofer Institute for Applied Optics and Precision Engineering IOF Jena, 07745 Jena, Germany; [f]Abbe Center of Photonics, Friedrich Schiller University Jena, 07745 Jena, Germany; [g]Department of Applied Physics, Royal Institute of Technology, SE-106 91 Stockholm, Sweden; [h]Single Quantum B.V., 2628 CJ Delft, The Netherlands; [i]Istituto Nazionale di Ricerca Metrologica, 10135 Turin, Italy; [j]European Laboratory for Non-Linear Spectroscopy (LENS), 50019 Sesto Fiorentino, Italy; [k]Department of Physics and Astronomy, University of Florence, 50019 Sesto Fiorentino, Italy; [l]Consiglio Nazionale delle Ricerche, 00185 Rome, Italy; [m]Center for Digital Safety & Security, Austrian Institute of Technology, 1210 Vienna, Austria; [n]College of Advanced Interdisciplinary Studies, National University of Defense Technology, Changsha 410073, China; [o]Quantum Optics, Quantum Nanophysics and Quantum Information, University of Vienna, 1090 Vienna, Austria; and [p]Department of Physics, University of Malta, Msida MSD 2080, Malta

Quantum entanglement is one of the most extraordinary effects in quantum physics, with many applications in the emerging field of quantum information science. In particular, it provides the foundation for quantum key distribution (QKD), which promises a conceptual leap in information security. Entanglement-based QKD holds great promise for future applications owing to the possibility of device-independent security and the potential of establishing global-scale quantum repeater networks. While other approaches to QKD have already reached the level of maturity required for operation in absence of typical laboratory infrastructure, comparable field demonstrations of entanglement-based QKD have not been performed so far. Here, we report on the successful distribution of polarization-entangled photon pairs between Malta and Sicily over 96 km of submarine optical telecommunications fiber. We observe around 257 photon pairs per second, with a polarization visibility above 90%. Our results show that QKD based on polarization entanglement is now indeed viable in long-distance fiber links. This field demonstration marks the longest-distance distribution of entanglement in a deployed telecommunications network and demonstrates an international submarine quantum communication channel. This opens up myriad possibilities for future experiments and technological applications using existing infrastructure.

quantum entanglement | quantum key distribution | quantum cryptography | polarization-entangled photons

Recent decades have established a solid physical basis for quantum key distribution (QKD) (1–5). Constant technological advancement has seen QKD extend to ever-longer distances (6, 7) and with increased key generation rates (8), linking cities (5, 9) and even continents via satellite links (10–13). Efforts are also well underway to extending QKD from point-to-point links to secure network infrastructures (9, 14–19).

Among various implementations of QKD, the entanglement-based approach is especially promising for future applications, as it forms the basis of device-independent quantum secure cryptography (20), holds the potential for yielding high bit rates, and facilitates networks without trusted nodes (19). Another form of entanglement-based QKD is measurement device-independent QKD (21–23), which already includes a Bell-state measurement required for full quantum repeated systems.

Despite the increasing level of maturity demonstrated in a variety of technological approaches to quantum cryptography, it remains necessary to demonstrate the robustness of entanglement distribution required for its deployment in industrially relevant environments. While the distribution of entanglement via

free space (24) and satellite links (25, 26) has seen tremendous advancement in the recent past, the vast majority of reported fiber-based experiments have been performed under idealized conditions, such as a fiber coil inside a single laboratory (27, 28). Notable exceptions include the distribution of time-bin–entangled photons over 10.9 km (29); this experiment was the first to distribute entangled photon pairs over deployed telecommunications fiber, and it was followed by distribution over 18 km (30). Polarization-entangled photon pairs have been distributed over 1.45 (31) and 16 km (32). Recently, quantum teleportation has been shown in deployed fiber networks using time-bin encoding over 16 km (33) and polarization-entangled photons (34) over 30 km. Entanglement swapping using time-bin encoding has also been shown over 100-km fiber, with the receivers being 12.5 km apart (35). Nevertheless, long-distance QKD based on polarization entanglement in deployed optical fiber links remains an outstanding challenge that must be addressed if such networks are to operate on existing infrastructure.

In this article, we report on the distribution of polarization-entangled photons via a standard fiber-based submarine

Significance

Entanglement, the existence of correlations in distant systems stronger than those allowed by classical physics, is one of the most astonishing features of quantum physics. By distributing entangled photon pairs over a 96-km-long submarine fiber, which is part of existing infrastructure carrying internet traffic, we demonstrate that polarization entanglement-based quantum key distribution (QKD) can be implemented in real-world scenarios. QKD facilitates secure communication links between two parties, whereby the security is guaranteed by the basic property of quantum mechanics that the quantum state of a photon cannot be duplicated.

telecommunications link between the Mediterranean islands of Malta and Sicily. The transmitter and receiver sites were separated by a distance of 93.4 km and lacked any form of laboratory infrastructure. Our results show that polarization entanglement is well preserved over long distances of fiber in a real-world scenario. Furthermore, the passive stability of the polarization state extends over hours, thus allowing a full implementation of QKD schemes over standard submarine telecommunication fibers.

The setup of our field demonstration is depicted in Fig. 1. A source of polarization-entangled photon pairs was located in Malta in the central data center of one of the local telecommunication providers (Melita Ltd.), close to Fort Madliena. One photon from each pair was sent to a polarization analysis and detection module located in Malta close to the source. This module consisted of a half-wave plate and a polarizing beam splitter with single-photon detectors connected to the transmitted and reflected output ports. The entangled partner photon was sent to Sicily via a 96-km-long submarine telecommunications optical fiber cable, which introduced an attenuation of about 22 dB. The link consists of several International Telecommunication Union (ITU) Telecommunication Standardization Sector G.655 compliant fibers, some of which were actively transmitting internet traffic in the C band around 1,550 nm. Two dark fibers within the same cable represented the quantum channel and a synchronization channel used to establish a common timing reference between time-tagging modules by an intensity-modulated diode laser. In Sicily, the fiber link was accessed through an underground utility vault on the outskirts of the town of Pozzallo. The fiber link was connected to a mobile polarization detection module installed in a stationary van and driven to the site each day.

The entangled photon source was based on spontaneous parametric down-conversion (SPDC) in a periodically poled type 0 lithium niobate (MgO:ppLN) crystal (*Materials and Methods* has details). The crystal was pumped from two directions within a Sagnac loop. The emitted down-converted photons were separated from the pump beam by a dichroic mirror. The source produced polarization-entangled signal and idler photons in the two-photon Bell state

$$|\Phi\rangle = \frac{1}{\sqrt{2}}(|V_{\lambda_s}V_{\lambda_i}\rangle - |H_{\lambda_s}H_{\lambda_i}\rangle),$$ [1]

where we denote the signal (idler) wavelength by λ_s (λ_i) and the polarization degree of freedom by horizontal (H) or vertical (V). Exploiting energy conservation in the SPDC process, the signal and idler photons were emitted with an equal spectral distance of the channels from the central wavelength of 1,550.15 nm. Following the terminology of the ITU, we chose the wavelength division multiplexing (WDM) channel 36 ($\lambda_s = 1,548.52$ nm) for the signal photons to be sent to Sicily, while the idler photons in channel 32 ($\lambda_i = 1,551.72$ nm) were detected locally in Malta. Superconducting nanowire single-photon detectors (SNSPDs) were used for the detection of the photons in Malta, while in Sicily, the detection system was more mobile and used single-photon avalanche detectors (SPADs) (*Materials and Methods* has more details on the detection system).

A signal generator located in Malta triggered a local time-tagging unit and modulated the intensity of a 1,550-nm laser, which synchronized the time-tagging unit in Sicily over a separate fiber. Each detection event was recorded by the respective time tagger and written to computer files locally and independently in Malta and Sicily. The two-photon coincidence events were identified by performing a cross-correlation between the photon detection times (Fig. 2), which can also be understood as a histogram of detection time delays.

Results

First, to quantify the quality of the entangled state after transmission through the submarine fiber, we performed a series of two-photon correlation measurements. In Sicily, the polarization analyzer was set to measure in either the H/V or diagonal (D)/antidiagonal (A) basis. The polarization angle ϕ_M analyzed in Malta was scanned from 0° to 360° in steps of 20°. For each angle setting in Malta, we accumulated data for a total of 60 s. The best-fit functions to the experimental data, two of which are shown in Fig. 3, exhibit a visibility of 86.8 ± 0.8%
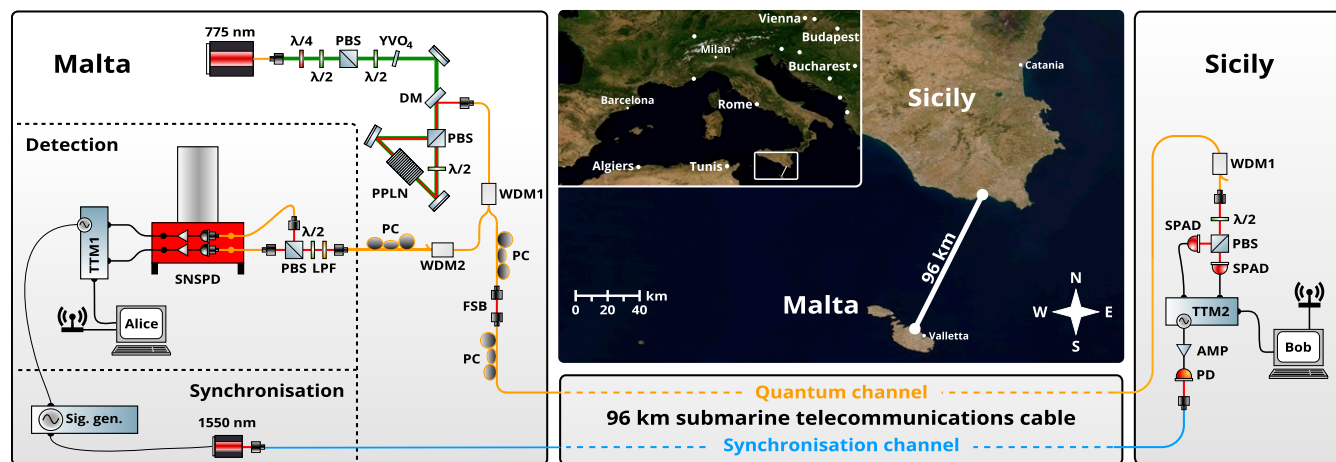
Fig. 1. Setup and location of the experiment. The fiber optic cable used here links the Mediterranean islands of Malta and Sicily. A continuous wave laser at 775 nm bidirectionally pumped an MgO-doped periodically poled lithium niobate crystal (MgO:ppLN; PPLN) crystal and created, via the process of spontaneous parametric down-conversion, photon pairs that are entangled in polarization due to the Sagnac geometry. Signal and idler photons are separated from the pump beam with a dichroic mirror (DM) and then split by frequency into two different fibers by the band-pass filters 100-GHz band-pass filter (center wavelength: 1,548.52 nm; WDM1) and 100-GHz band-pass filter (center wavelength: 1,551.72 nm; WDM2); one photon is detected locally in Malta in a polarization analysis module consisting of a half-wave plate in front of a polarizing beam splitter (PBS) and two SNSPDs. The other photon is detected by SPADs in Sicily after transmission through the 96-km submarine telecommunications fiber. Mirrors and fiber couplers are not labeled, lenses are omitted. TTM1 and TTM2 are time-tagging modules, and λ/4 and λ/2 are wave plates. AMP, 50-dB voltage amplifier; LPF, 780-nm long-pass filter; PC, fiber polarization controller; PD, fast InGaAs photodiode; Sig. gen., 10-MHz signal generator; YVO₄, yttrium orthovanadate plate. Map images courtesy of NASA Worldview.
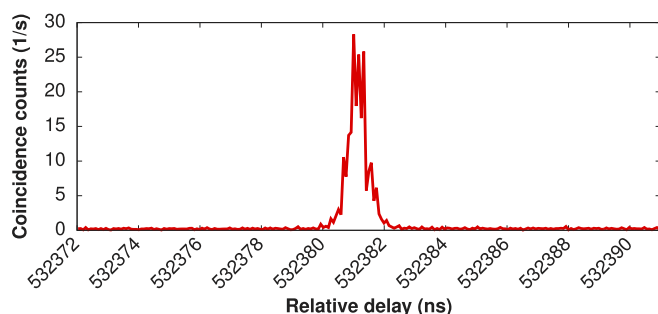
Fig. 2. The cross-correlation function between the time tags from Malta and Sicily shows a peak at a relative delay of ~532,281 ns, which corresponds to the length of the fiber when we take into account the different latencies of the detection systems. Coincident events are counted if they fall within 500 ps from the central peak position. The FWHM of ~0.7 ns is attributed to timing uncertainty of the SPADs in Sicily (~400 ps), the dispersion of the fiber link (~500 ps), and other effects dominated by the timing uncertainty of the time-tagging units and their synchronization (<300 ps), including the uncertainty of the SNSPD system in Malta (<100 ps).

in the H/V basis and $94.1 \pm 0.2\%$ in the D/A basis. Second, to further quantify the quality of polarization entanglement, we combined the results of the coincidence scans to yield the Clauser–Horne–Shimony–Holt (CHSH) quantity $S(\phi_M)$, which is bounded between -2 and 2 for local realistic theories but may exceed these bounds up to an absolute value of $2\sqrt{2}$ in quantum mechanics (36). To mitigate against systematic errors due to misalignment of the polarization reference frames, we used a best fit to the coincidence data (e.g., as shown in Fig. 3) to compute $S(\phi_M)$ as shown in Fig. 4. We observed the maximum Bell violation for a CHSH value of -2.534 ± 0.08, which corresponds to ~90% of the Tsirelson bound (37) and is in good agreement with the visibility of the two-photon coincidence data. Note that this value was obtained for $\phi_M = 63.5°$, which corresponds to an offset of $4.0°$ from the theoretical optimum $(67.5°)$. We ascribe this difference to a residual error in setting the zero point of our wave plates and imperfect compensation of the birefringence of the submarine fiber. Another factor that contributes to the imperfect visibility is the accidental identification of coincident pairs, which reduced the visibility by ~3.5%. The polarization mode dispersion is specified to be around 0.4 ps (38), and its effect on the visibility can be neglected (39). In an additional measurement run, we directly measured the CHSH inequality for angle settings $22.5° - 157.5°$ and H/V–D/A (Malta–Sicily), respectively. In this case, we observe a CHSH value of 2.421 ± 0.008 as illustrated by the green horizontal line in Fig. 4. This is well beyond the bounds imposed by local realistic theories.

Third, another experiment was made to check the feasibility of implementing QKD over this submarine fiber link, despite not having implemented a fast and random basis choice on both sides. Instead, we used the two motor-driven rotation stages on both sides to set the half-wave plates once to $0°$ (H/V) and once to $22.5°$ (D/A) basis. From the measured data, we estimated the secure key rate that would have been observed if we had implemented a random basis choice, and coincidence count rates for the case of close-to-perfect correlations were measured separately in the H/V and D/A bases. The total coincidence rate for all four combinations of detectors was between 248 counts per second in the H/V basis and 257 counts per second in the D/A basis at quantum bit error rates (QBERs) of 5 and 3%, respectively (40). After 2.9 s of measurement, the secret key rate would have been positive (41, 42). In the asymptotic time limit, the key rate achieved would be about 57.5 bits per second.

Discussion

Our results demonstrate the successful distribution of entanglement over a 96-km-long submarine optical fiber link that is part of actively used classical telecommunications infrastructure. This field demonstration marks the longest-distance distribution of entanglement in a deployed telecommunications network and demonstrates an international submarine quantum communication channel. We verified the quality of entanglement by violating the CHSH inequality at the level of 86% (2.421) and have demonstrated all of the quantum prerequisites to be able to fully implement QKD with rates of 57.5 bits per second in the asymptotic time limit. The link attenuation and QBER stayed constant for over 2.5 h without active polarization stabilization. This is in accordance with results from other groups that investigated the changes of the polarization state of buried fibers (43) and found slow drifts on the scale of hours or days. These slow drifts could be compensated for periodically by using an alignment signal as in ref. 32. The stability depends on the external conditions, since sometimes, buried or aerial fibers are found to exhibit faster polarization changes (23, 44, 45), which call for a control technique that continuously optimizes the QBER.

Based on this, we can conclusively prove that secure polarization entanglement-based quantum communication is indeed possible over comparable deployed fiber links.

While most field demonstrations of quantum cryptography in fiber were based on time-bin encoding (40, 46), our field trial was based on polarization encoding. Our results highlight the convenience of polarization-entangled qubits for future implementations of QKD networks. This is because polarization-entangled qubits are easy to measure and prepare with a high fidelity, and they can be transmitted without notable depolarization over distances of at least ~100 km as indicated by our experimental results. Nevertheless, studies mentioned above (23, 43, 44, 45) have shown that the deployed fibers have to be selected with care, as the stability of their polarization state depends on external influences. Polarization entanglement can also be used to seamlessly interface between free space- and fiber-based communication links. Finally, one can simply make use of the many quantum repeater and quantum networking schemes that have been proposed for polarization entanglement, which can further extend the range of QKD systems and the number of clients that they can reach. As an outlook, we note that, by using commercially available detectors with improved timing resolution (47), we could more than double the distance with respect to this experiment. Our work thus opens up the
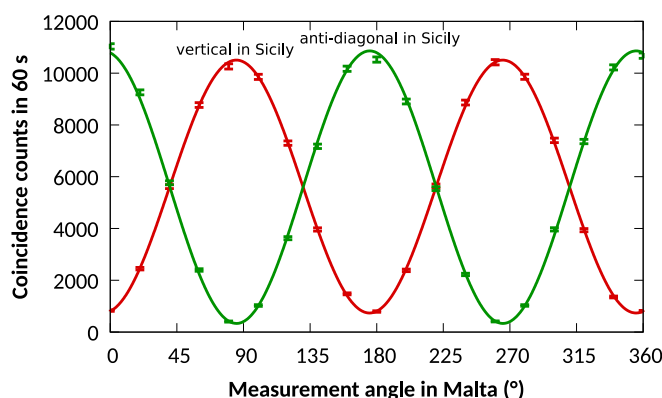
Fig. 3. Coincidence count rates for one detector pair and two different measurement angles in Sicily [V (red) and A (green)] as a function of the measurement angle for the analyzer in Malta, ϕ_M, starting from H (red) or D (green). Poissonian statistics are assumed for the data as indicated by the error bars.
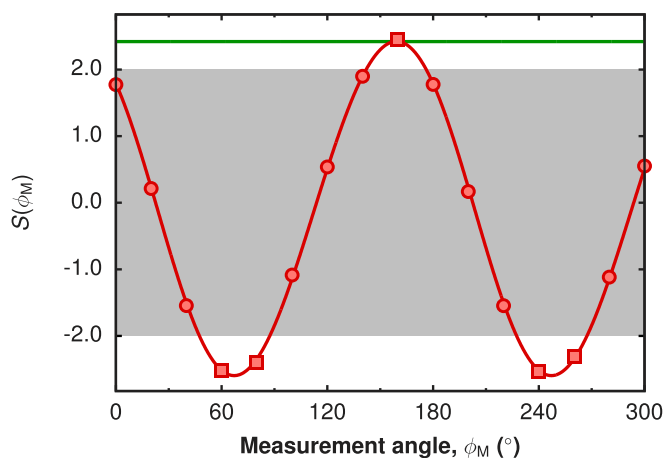
Fig. 4. CHSH quantity $S(\phi_M)$ as a function of the measurement angle for the analyzer in Malta, ϕ_M, which resembles the relative angle between the two mutually unbiased bases that were used in Malta and Sicily each. Error bars are included but fit within the data markers; the SD is ≤ 0.014 for all of the points shown. Data outside the gray region (shown as squares) exclude local realistic theories. This function is computed using data similar to those shown in Fig. 3. The solid red curve is obtained from a fit to the coincidence rates (as in Fig. 3) and not from a fit to the data shown here, and it yields a CHSH value of 2.534 ± 0.08. The green horizontal line shows the CHSH value of 2.421 ± 0.008 obtained in a measurement run at the fixed value of $\phi_M = 157.5°$ (this includes a measurement at $22.5°$; i.e., the theoretically optimal angles).

possibility of using polarization entanglement for truly global-scale fiber-based quantum communication.

Materials and Methods

Entangled Photon Source. The source of polarization-entangled photons was based on spontaneous parametric down-conversion in a periodically poled lithium niobate (MgO:ppLN) crystal. To produce signal and idler pairs spanning in the telecommunications C band, type 0 quasiphase matching was used to produce, from a continuous wave pump laser with the wavelength 775.075 nm, signal and idler pairs in the telecommunication C band. The MgO:ppLN crystal was bidirectionally pumped inside a Sagnac-type setup (48) to produce the polarization-entangled Bell state. The pump power was set to 21.3 mW for the visibility measurement, 23.9 mW for the CHSH measurements, and 25.5 mW for the key rate measurement.

Due to conservation of energy during the down-conversion process from a well-defined pump energy, polarization-entangled photon pairs are found at equal spectral distance from the central frequency. We used $\sim$0.6-nm FWHM band-pass filters to separate signal and idler photons at an equal spectral distance of the channels from the central wavelength of 1,550.15 nm. ITU WDM channel 36 ($\lambda_s = 1,548.52$ nm) was chosen for the signal photons to be sent to Sicily, while the idler photons in channel 32 ($\lambda_i = 1,551.72$ nm) were detected locally in Malta.

Locally in Malta, the visibility of the source was measured at $\sim$98% in the D/A polarization basis and 97% in the H/V basis. The local heralding efficiency was $\sim$12% measured on the SNSPD system; locally, 28,000 pairs were detected per milliwatt of pump power. Two SNSPDs, necessary for handling the high count rates of 1.3 and 1.93 million counts per second, were used in the detection system in Malta, and they were operated at efficiencies of $\sim$54 and 59%, respectively, and with dark count rates of $\sim$550 and 470 counts per second, respectively.

Fiber Birefringence Compensation. The $|\Phi\rangle$ state was optimized locally in Malta by changing the polarization of the pump beam and characterized using the local detection module and a polarization analysis module that was inserted into the region denoted free space beam (FSB) in Fig. 1. To ensure that the quantum state can be detected at the other end of the 96-km fiber link, the polarization rotation of the quantum channel was neutralized by receiving alternately one of two mutually unbiased polarization states H and D from a laser, which was connected in the place of an SPAD in Sicily. The neutralization was done manually using the signal

of a polarimeter placed in the region FSB and manual fiber polarization controllers.

Single-Photon Counting in Malta. The superconducting detectors used in Malta were fabricated from a newly developed 9-nm-thick NbTiN superconducting film deposited by reactive cosputtering at room temperature at the Swedish Royal Institute of Technology. The nanowires were patterned using electron beam lithography and subsequent dry etching in collaboration with Single Quantum. The fabrication process included additional fabrication steps, such as back-mirror integration and through-wafer etching for fiber alignment. We used a commercial cryostat (Single Quantum Eos) operating at 2.9 K and a current driver (Single Quantum Atlas) to operate the fiber-coupled SNSPDs. The efficiency of the detectors being dependent on the photon polarization, a three-paddle fiber polarization controller was used to optimize the detection efficiency. The SNSPD system operated continuously for 2 weeks in a data center facility at an ambient temperature of about 30 °C without any degradation in performance.

Single-Photon Counting in Sicily. In Sicily, two different models of free-running SPADs based on InGaAs were used due to their greater mobility compared with the cryogenic SNSPDs. However, they presented very different characteristics than the SNSPDs used in Malta in terms of efficiency and dark counts. One detector had an efficiency of $\sim$2–4% at a dead time of 1 μs and $\sim$140 dark counts per second, while the other operated at an efficiency of $\sim$10% at a dead time of 5 μs with $\sim$550 dark counts per second. The count rates including dark counts were between 590 and 890 counts per second for the detector with lower efficiency and between 2,100 and 2,300 counts per second for the detector with higher efficiency.

CHSH Measurements. To compute the S value, measurements from four basis settings were combined, while coincidence counts between all four detectors were used. The CHSH inequality reads

$$-2 \leq S = E(a_1, b_1) + E(a_1, b_2) + E(a_2, b_1) - E(a_2, b_2) \leq 2, \quad [2]$$

while a_i with $i = 1, 2$ indicates the angles in Malta with $a_1 - a_2 = 45°$ and $b_1 - b_2 = 45°$ in Sicily. The correlation functions $E(a_i, b_i)$ are computed from the coincidence counts $C(a_i, b_j)$ measured at the angles a_i, b_j as follows:

$$E(a_i, b_i) = \frac{C(a_i, b_j) + C(a_{i\perp}, b_{j\perp}) - C(a_{i\perp}, b_j) - C(a_i, b_{j,\perp})}{C(a_i, b_j) + C(a_{i\perp}, b_{j\perp}) + C(a_{i\perp}, b_j) + C(a_i, b_{j,\perp})}. \quad [3]$$

The symbol $\perp$ corresponds to the perpendicular angle (i.e., the second output of the polarizing beam splitter). The angle ϕ_M in Fig. 4 can be understood as the relative angle between the measurement bases used in Malta and Sicily and is proportional to $a_i - b_i$.

We measured the CHSH value with the analyzers set to the expected optimal settings $22.5° - 157.5°$ and H/V–D/A (Malta–Sicily), respectively. For each measurement setting, we accumulated data for a total of 600 s. They provided enough data to break down the data series into 39 blocks per measurement setting and perform a statistical analysis of the data without relying on Poissonian count rate statistics.

Estimation of Finite Secret Key Rate. The secret key rate given in the text has been estimated based on the assumption that the setup had used a fast and random basis choice for each photon arriving at the detector. For that, two measurements of 15 s have been made, one in the D/A basis and one in the H/V basis, to estimate the QBER for each basis. In total, this gives sifted key lengths of 3,730 bits in the H/V basis and 3,857 bits in the D/A basis, which would have been measured in 60 s if the basis had switched fast and randomly. The error counts were 196 and 118 bits, respectively. The count rates observed over 15 s have been scaled to other timescales to estimate the finite-size key rate. The finite-size effect considered here is due to the fluctuations of the count rate that increase the phase error. The phase errors θ_x and θ_z have been estimated using the relations given in ref. 42, such that the probability p_{θ_i} to underestimate the phase error rate is smaller than 10^{-5}. This allows us to calculate the key rate using an expression from ref. 41 with an error correction efficiency of 1.2 (49). After 2.9 s of measurement, the secret key rate would have been positive (41, 42), and after 60 s, the rate would be around 46 bits per second. In the asymptotic time limit, the key rate achieved is about 57.5 bits per second.

PHYSICS

1. Bennett C, Bessette F, Brassard G, Salvail L, Smolin J (1992) Experimental quantum cryptography. *J Cryptol* 5:3–28.
2. Jennewein T, Simon C, Weihs G, Weinfurter H, Zeilinger A (2000) Quantum cryptography with entangled photons. *Phys Rev Lett* 84:4729–4732.
3. Naik DS, Peterson CG, White AG, Berglund AJ, Kwiat PG (2000) Entangled state quantum cryptography: Eavesdropping on the Ekert protocol. *Phys Rev Lett* 84:4733–4736.
4. Tittel W, Brendel J, Zbinden H, Gisin N (2000) Quantum cryptography using entangled photons in energy-time bell states. *Phys Rev Lett* 84:4737–4740.
5. Muller A, Zbinden H, Gisin N (1996) Quantum cryptography over 23 km in installed under-lake telecom fibre. *Europhys Lett (EPL)* 33:335–340.
6. Korzh B, et al. (2015) Provably secure and practical quantum key distribution over 307 km of optical fibre. *Nat Photon* 9:163–168.
7. Yin HL, et al. (2016) Measurement-device-independent quantum key distribution over a 404 km optical fiber. *Phys Rev Lett* 117:190501.
8. Dixon AR, Yuan ZL, Dynes JF, Sharpe AW, Shields AJ (2008) Gigahertz decoy quantum key distribution with 1 Mbit/s secure key rate. *Opt Express* 16:18790–18797.
9. Wang M (2017) CAS center for excellence in quantum information and quantum physics: Exploring frontiers of quantum physics and quantum technology. *Natl Sci Rev* 4:144–152.
10. Liao SK, et al. (2017) Satellite-to-ground quantum key distribution. *Nature* 549:43–47.
11. Liao SK, et al. (2018) Satellite-relayed intercontinental quantum network. *Phys Rev Lett* 120:030501.
12. Takenaka H, et al. (2017) Satellite-to-ground quantum-limited communication using a 50-kg-class microsatellite. *Nat Photon* 11:502–508.
13. Günther K, et al. (2017) Quantum-limited measurements of optical signals from a geostationary satellite. *Optica* 4:611–616.
14. Stucki D, et al. (2011) Long-term performance of the SwissQuantum quantum key distribution network in a field environment. *New J Phys* 13:123001–123019.
15. Sasaki M, et al. (2011) Field test of quantum key distribution in the Tokyo QKD network. *Opt Express* 19:10387–10409.
16. Peev M, et al. (2009) The SECOQC quantum key distribution network in Vienna. *New J Phys* 11:075001–075038.
17. Elliott C, et al. (2005) Current status of the DARPA quantum network. *Proceedings of the SPIE 5815, Quantum Information and Computation III*, eds Donkor EJ, Pirich AR, Brandt HE (SPIE, Orlando, FL), Vol 5815, pp 138–149.
18. Wang S, et al. (2014) Field and long-term demonstration of a wide area quantum key distribution network. *Opt Express* 22:21739–21756.
19. Wengerowsky S, Joshi SK, Steinlechner F, Hübel H, Ursin R (2018) An entanglement-based wavelength-multiplexed quantum communication network. *Nature* 564:225–228.
20. Masanes L, Pironio S, Acín A (2011) Secure device-independent quantum key distribution with causally independent measurement devices. *Nat Commun* 2:238.
21. Lo HK, Curty M, Qi B (2012) Measurement-device-independent quantum key distribution. *Phys Rev Lett* 108:130503.
22. Liu Y, et al. (2013) Experimental measurement-device-independent quantum key distribution. *Phys Rev Lett* 111:130502.
23. Rubenok A, Slater JA, Chan P, Lucio-Martinez I, Tittel W (2013) Real-world two-photon interference and proof-of-principle quantum key distribution immune to detector attacks. *Phys Rev Lett* 111:130501.
24. Nagali E, D'Ambrosio V, Sciarrino F, Cabello A (2012) Experimental observation of impossible-to-beat quantum advantage on a hybrid photonic system. *Nat Phys* 3:481–486.
25. Yin J, et al. (2017) Satellite-based entanglement distribution over 1200 kilometers. *Science* 356:1140–1144.
26. Ren JG, et al. (2017) Ground-to-satellite quantum teleportation. *Nature* 549:70–73.
27. Hübel H, et al. (2007) High-fidelity transmission of polarization encoded qubits from an entangled source over 100 km of fiber. *Opt Express* 15:7853–7862.
28. Inagaki T, Matsuda N, Tadanaga O, Asobe M, Takesue H (2013) Entanglement distribution over 300 km of fiber. *Opt Express* 21:23241–23249.
29. Tittel W, Brendel J, Zbinden H, Gisin N (1998) Violation of bell inequalities by photons more than 10 km apart. *Phys Rev Lett* 81:3563–3566.
30. Salart D, Baas A, Branciard C, Gisin N, Zbinden H (2008) Testing the speed of 'spooky action at a distance.' *Nature* 454:861–864.
31. Poppe A, et al. (2004) Practical quantum key distribution with polarization entangled photons. *Opt Express* 12:3865–3871.
32. Treiber A, et al. (2009) A fully automated entanglement-based quantum cryptography system for telecom fiber networks. *New J Phys* 11:045013–045032.
33. Valivarthi R, et al. (2016) Quantum teleportation across a metropolitan fibre network. *Nat Photon* 10:676–680.
34. Sun Q, et al. (2016) Quantum teleportation with independent sources and prior entanglement distribution over a network. *Nat Photon* 10:671–675.
35. Sun Q-C, et al. (2017) Entanglement swapping over 100 km optical fiber with independent entangled photon-pair sources. *Optica* 4:1214–1218.
36. Clauser JF, Horne MA, Shimony A, Holt RA (1969) Proposed experiment to test local hidden-variable theories. *Phys Rev Lett* 23:880–884.
37. Cirel'son BS (1980) Quantum generalizations of Bell's inequality. *Lett Math Phys* 4:93–100.
38. Corning (2014) Corning leaf data sheet. Available at https://www.corning.com/media/worldwide/coc/documents/Fiber/LEAF%20optical%20fiber.pdf. Accessed November 28, 2018.
39. Brodsky M, George EC, Antonelli C, Shtaif M (2011) Loss of polarization entanglement in a fiber-optic system with polarization mode dispersion in one optical path. *Opt Lett* 36:43–45.
40. Gisin N, Ribordy G, Tittel W, Zbinden H (2002) Quantum cryptography. *Rev Mod Phys* 74:145–195.
41. Ma X, Fung CHF, Lo HK (2007) Quantum key distribution with entangled photon sources. *Phys Rev A* 76:012307.
42. Fung CHF, Ma X, Chau H (2010) Practical issues in quantum-key-distribution postprocessing. *Phys Rev A* 81:012318.
43. Ding Y-Y, et al. (2017) Polarization variations in installed fibers and their influence on quantum key distribution systems. *Opt Express* 25:27923–27936.
44. Yoshino K, Ochi T, Fujiwara M, Sasaki M, Tajima A (2013) Maintenance-free operation of wdm quantum key distribution system through a field fiber over 30 days. *Opt Express* 21:31395–31401.
45. Waddy DS, Chen L, Bao X (2005) Polarization effects in aerial fibers. *Opt Fiber Technol* 11:1–19.
46. Gisin N, Thew R (2007) Quantum communication. *Nat Photon* 1:165–171.
47. Zadeh IE, et al. (2018) A single-photon detector with high efficiency and sub-10ps time resolution. arXiv:1801.06574.
48. Taehyun K, Fiorentino M, Wong FNC (2006) Phase-stable source of polarization-entangled photons using a polarization Sagnac interferometer. *Phys Rev A*, 73:012316.
49. Ma X, et al. (2006) Decoy-state quantum key distribution with two-way classical postprocessing. *Phys Rev A* 74:032330.